

Modeling Solid-Particle Erosion of Ductile Alloys

B.F. LEVIN, K.S. VECCHIO, J.N. DuPONT, and A.R. MARDER

A model for solid-particle erosion behavior of ductile alloys is presented. The model incorporates the mechanical properties of the alloys at the deformation conditions associated with solid-particle erosion processes (*i.e.*, temperature and strain-rate conditions), as well as the evolution of these properties during the erosion-induced deformations. An erosion parameter was formulated based on consideration of the energy loss during erosion and incorporates the material's hardness, along with the high-strain-rate stress-strain response of the alloy. This erosion parameter shows a good correlation to experimentally measured erosion rates for a variety of industrially important materials. A methodology is presented to determine the proper mechanical properties to incorporate into the erosion parameter based on a physical model of the erosion mechanism in ductile materials.

I. INTRODUCTION

SOLID-particle erosion is a loss of material during repetitive impacts of solid particles and is one of the primary reasons for fly ash-borne damage of power generation components. A description of the erosion mechanism in terms of the mechanical properties was presented by Bitter.^[1] During impact, when the yield strength of the material is locally exceeded, plastic deformation takes place in the vicinity of the impact. After multiple impacts, a plastically deformed surface layer may form near the eroded surface, and, therefore, the yield strength of the material increases due to strain hardening. Upon further deformation, the yield strength at the surface of the material will eventually become equal to its fracture strength, and no further plastic deformation will occur. At this point, the material surface becomes brittle and its fragments may be removed by the subsequent impacts. Some researchers have suggested that, during erosion, material loss from a metal surface occurs when a critical fracture strain is achieved at the surface.^[2] A critical fracture strain may be achieved locally after single or multiple impacts by the erodent particles. As material is lost at the attainment of the critical strain, the material below the surface is still plastically yielding. Ball^[3] proposed that, in order to design a material to resist erosion, attention must be given to providing a microstructure that, ideally, never accumulates the critical fracture strain under the stress that the impacting particles impose. Therefore, the ability of a material to accommodate impact energy may contribute to its erosion resistance.

Many studies have been conducted to determine the effect of mechanical properties, chemical composition, and the microstructure of various materials on their erosion resistance. However, good correlations between these parameters have been obtained only within narrow classes of materials. By determining the effects of mechanical properties on erosion resistance, the microstructure of a given alloy could be

optimized to provide the best combination of mechanical properties for erosion protection. Hardness is the most widely used property to correlate with the erosion rates of materials. For pure metals, some correlation between erosion rate and hardness has been shown.^[4] However, several other observations have shown that the erosion rate is not dependent on material hardness.^[5,6] Hutchings^[7] proposed that the effect of hardness on erosion resistance is strongly dependent on the properties of the erosive particles and erosion test conditions (velocity, shape, size, and density of the particles). When hard angular particles strike a relatively soft target, the target surface will deform plastically. On the other hand, when soft erodent particles are used, they may fracture upon impact. In this case, erosion damage will decrease as the target hardness increases. In addition, the effect of hardness on erosion resistance depends on the velocity of the erosive particles. For example, it was established that the critical particle velocity below which plastic deformation of the target does not occur is proportional to the target hardness.^[8] This relationship is given by

$$V_c = 4.3 \cdot H^{2.5} \cdot J^2 \cdot \rho^{-0.5} \quad [1]$$

where V_c is the critical velocity, H is the hardness of the target material, J is a parameter that depends on the elastic modulus of the target and the particle materials, and ρ is the density of the impacting particle. Based on this equation, it can be suggested that, at low particle velocities ($V_p < V_c$), materials with high hardness may offer good erosion resistance, because impacting particles may not produce plastic deformation and/or cracking of the target material. However, at high particle velocities ($V_p > V_c$), when plastic deformation and/or cracking are common, hardness may not improve the erosion resistance of the target. In spite of many attempts to correlate hardness to the erosion resistance of various alloys, no adequate quantitative relationship was obtained. It is clear that the effect of hardness on erosion resistance must be considered in relation to the erodent properties (*i.e.*, size, shape, and density) and erosion test conditions (*i.e.*, velocity, temperature, and angle of impact).

Hutchings^[9] proposed that cyclic fatigue is the dominant mechanism of material removal during erosion and derived an equation to predict erosion resistance. In this model, the erosion resistance is proportional to $H^{3/2} \epsilon_c^2$, where H is the material hardness and ϵ_c is the critical strain to fracture. Other models were proposed to correlate erosion resistance

B.F. LEVIN is Staff Engineer with A.T. Kearney, Inc., Chicago, IL 60609. K.S. VECCHIO, Associate Professor of Materials Science, is with the Mechanical and Aerospace Engineering Department, University of California, San Diego, La Jolla, CA 92093-0411. J.N. DuPONT, Research Scientist, Energy Research Center, and A.R. MARDER, Professor, Materials Science and Engineering Department, Whitaker Lab, are with Lehigh University, Bethlehem, PA 18015.

Manuscript submitted May 14, 1998.

to material properties such as hardness or yield strength^[10] and the amount of energy transferred into the material during particle impact.^[11] Although these models showed a reasonable correlation to erosion resistance for different alloys, their major simplification is a neglect of work hardening in ductile materials during particle impacts. In these models, it was assumed that materials had constant mechanical properties during erosion (*i.e.*, hardness, yield strength, and fracture strain). However, because of work hardening, the material hardness will increase in the vicinity of the eroded surface, and the strain introduced by each impact will be reduced. As such, efforts to model erosion behavior of ductile materials without considering the effect of work hardening do not accurately represent the mechanism of material removal.

Only a few attempts have been made to measure the plastic-zone size that forms in ductile materials in the vicinity of the eroded surface.^[12,13,14] This is particularly surprising, since the size of the plastically deformed region may represent a measure of energy absorbed before fracture during erosion; only one erosion model^[14] accounted for the plastic-zone size. Assuming that the plastic-zone depth is proportional to the size of the crater that forms during impact, it was concluded that the erosion rate is proportional to L^3 (L is the plastic-zone depth). However, this model contains several parameters that are not readily measurable and, therefore, its applicability for selection of erosion-resistant materials is limited. Moreover, the assumed relationship between the plastic-zone depth and crater volume needs to be verified.

To develop a quantitative model for erosion of ductile materials, it is essential to consider the energy balance during particle impact. The investigation of the relationship between the erosion resistance and the energy transmitted from the impacting particle into the target material may be a useful approach for the development of the erosion model. Energy that is *actually transferred* into the material depends on the mechanical properties of the material, such as hardness, yield strength, strain-hardening coefficient, modulus, *etc.* Assuming that the particle does not fracture or deform upon impact with the target material, its kinetic energy is transferred to elastic and plastic deformation of the target. Most of the elastic energy is released to produce particle rebound, while plastic deformation energy is used to form a plastic zone beneath the eroded surface. The size of the plastically deformed region may provide an estimate of the material's ability to absorb particle impact energy. In order to determine the effect of mechanical properties on erosion resistance, their effect on the plastic-zone size that forms during erosion must be investigated.

Finally, the development of an erosion model requires consideration of the strain-rate sensitivity of a material's mechanical properties. During erosion, the particles impose high-strain-rate deformation on the material. The erosion process involves strain rates on the order of 10^3 to 10^6 s^{-1} .^[15] In contrast, the mechanical properties of a material are typically measured from low-strain-rate (quasi-static, 10^{-4} to 10^{-2} s^{-1}) tensile tests. Therefore, if a material is strain-rate sensitive, the mechanical properties measured from a quasi-static tensile test may be significantly different from those associated with solid-particle erosion. It is the purpose of this research to develop a correlation between the *high-strain-rate* mechanical properties of various ductile

alloys and their experimentally measured solid-particle erosion resistance.

II. EXPERIMENTAL PROCEDURE

A. Materials

The erosion behavior and mechanical properties of several Ni-, Co-, and Fe-based wrought alloys (Ultimet, INCONEL*-625, HASTELLOY**-C22, HAYNES**-B3,

*INCONEL is a trademark of INCO Alloys International, Huntington, WV.

**HASTELLOY and STELLITE are trademarks of Stoodly Deloro Stellite, Inc., Industry, CA. HAYNES is a trademark of Haynes International, Kokomo, IN.

STELLITE**-6, and 316L SS) and commercially pure Cu and Ni were analyzed. All of the alloy materials were austenitic, solid solution-strengthened alloys and provided a broad variation in mechanical properties. The Stellite-6 alloy contained approximately 20 vol pct of hard carbides in a ductile austenitic matrix. The chemical compositions were determined by optical emission spectroscopy and are shown in Table I. Each material was obtained in the form of fully annealed, rolled bar stock, and the experiments discussed subsequently were carried out on the materials in the as-received condition.

B. Erosion Testing

The solid-particle erosion testing system used in this study is described in detail elsewhere.^[16] The system is driven by an air compressor that can deliver up to 1.65×10^{-2} m^{-3} s^{-1} (35 cfm) of air at 8.62×10^{-5} Pa (125 psi). A pressure regulator and a flow meter control the amount of air flowing through the system. Two in-line fluid heaters can heat the air to temperatures up to 700° C upon exiting the heaters. A thermocouple is located directly after the heaters and is used by the heater control unit to maintain the set-point temperature. An erodent is fed into the air stream with a screw feeder driven by a variable-speed motor. A storage hopper sits above the feeder, and both the hopper and feeder employ gas-tight seals to ensure constant feed rates that are independent of airflow. The screw feeder can handle particles ranging in size from <50 μm to ~ 1.5 mm.

The particles and air are forced into a SiC acceleration tube that measures 1.5 m in length and 15 mm in diameter. A tube furnace with a maximum temperature of 1200 °C surrounds the acceleration tube. A long acceleration tube is used to ensure that the particles have reached the velocity of the gas prior to impact. Particle velocity is measured with a laser doppler velocimeter (LDV) upon exiting the acceleration tube. This technique allows for direct measurement of the particle velocity without disturbing the particle flow. The erosion samples are held under the particle stream by a sample holder, which can be pivoted to any angle about the axis of rotation, so that any impingement angle (0 deg $< \alpha \leq 90$ deg) can be tested. The impingement angle is measured as the angle between the particle stream and the target surface. Due to the high velocity of the air stream, erodent and erosion debris are continually removed from the target surface during testing.

The specimen chamber was fabricated from austenitic

Table I. Chemical Composition (Weight Percent) of the Selected Alloys

Alloy	Co	Cr	Fe	Mn	Mo	Ni	W	Cu	Other
Ultimet	bal	25.5	3.0	0.8	4.3	8.9	1.3	—	0.24Si, 0.07C
INCONEL-625	—	21.6	4.4	0.03	8.9	bal	—	—	3.49Nb, 0.26Ti, 0.15Al, 0.02C
HASTELLOY-C22	1.8	21.6	5.0	0.23	13.8	bal	2.9	—	0.18V, 0.007C
316L SS	—	17.3	bal	1.5	2.0	11.0	—	—	0.02C, 0.5Si
HAYNES-B3	—	1.2	—	0.54	27.2	69.0	—	—	0.34Al
STELLITE-6	bal	32.6	1.0	1.2	0.9	2.7	4.4	—	1.1C, 0.6Si
Nickel 200	—	—	0.1	0.24	—	bal	—	0.01	0.01C, 0.03Si
Copper	—	—	—	—	—	0.044	—	99.9	0.01P

stainless steel and has six openings. An opening in the top allows the acceleration tube to penetrate into the chamber so that the end of the tube is 2.54 cm from the sample. The bottom opening is the exhaust tube that leads to the cyclone for debris recovery. On three sides of the chamber are portals that contain quartz windows. These windows serve two functions: (1) to allow the laser beam from the LDV system to pass through the chamber with minimum distortion and (2) to allow visual access to the chamber. On the final side of the chamber is the door. The manipulator-rod assembly passes through this door and is sealed by the bellows. A thermocouple feed-through is also located on the door, for temperature measurements during testing and calibration.

The standard test conditions chosen for this study are listed in Table II. At least five different erosion exposure times, ranging from 30 to 240 minutes, were used in this study to adequately obtain the weight loss vs time plot for each material. The slopes of these plots yield the material's steady-state erosion rate. To quantify weight loss during the erosion experiments, the erosion specimens were ultrasonically cleaned in acetone and weighed before and after the erosion tests to the nearest 0.1 mg. The volumetric erosion rate for each alloy was obtained by dividing the weight loss rate by the density of the alloy. Only fresh Al_2O_3 particles were used for the erosion tests (*i.e.*, particles were not reused).

C. Microhardness Testing

To determine the size of the deformed region beneath the eroded surface and the maximum hardness at the eroded surface, microhardness tests were performed on a cross section of each eroded test specimen after the longest exposure time of 240 minutes. A depth of plastic deformation was determined by obtaining a microhardness profile from the eroded surface into the base material; a schematic diagram of this profile is shown in Figure 1. The depth at which the hardness value becomes constant is defined as a plastic-zone size. All measurements were performed using a Knoop

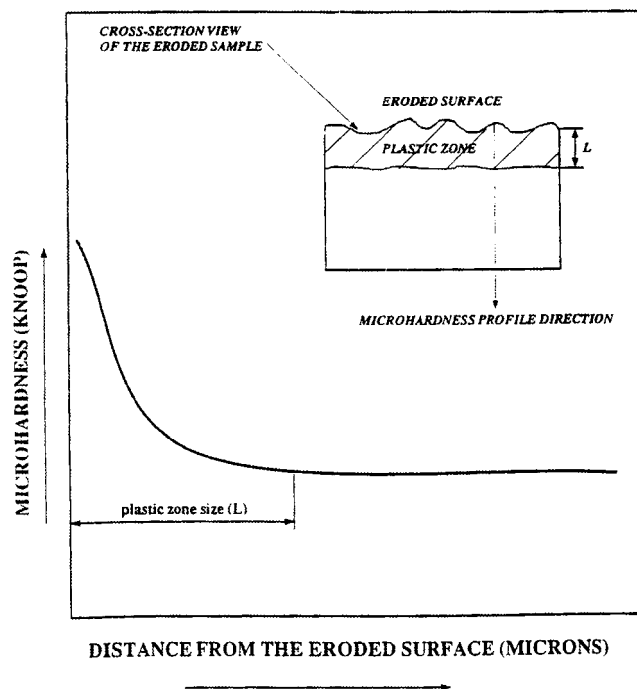


Fig. 1—Schematic diagram of the microhardness technique that was used to measure plastic deformation below the eroded surface.

indenter with a test load of 10 g. The Knoop indenter minimizes the specimen edge effect on microhardness results, allowing the tests to begin at 5 to 10 μm from the eroded surface. Three to five microhardness profiles were obtained at different locations of each material in order to improve the statistical significance of the data. Figure 2 shows a light optical micrograph of a cross section specimen, showing the microhardness indentations leading up to the eroded surface.

D. Mechanical Testing

Compression tests in the quasi-static regime were conducted on a conventional servohydraulic test frame, and tests in the high-strain-rate regime were conducted using a compression split-Hopkinson pressure bar. Compression specimens were machined from each material as right, regular cylinders having a diameter of 5.08 mm and a height of 5.08 mm. A detailed discussion of classical Hopkinson-bar techniques and recent experimental modifications can be found elsewhere.^[17,18] For the elevated-temperature tests conducted at high strain rates, the specimens were heated by a small tube furnace attached to the split-Hopkinson bar

Table II. Erosion Test Conditions

Eroded sample planar dimensions	0.95 × 0.95 cm, surface area $\approx 9 \times 10^{-5} m^2$
Sample temperature	20 °C
Erodent particle velocity	40 m/s, ± 3 m/s
Erodent particles flux	8.50 mg/(mm ² /s)
Impingement angle	90 deg
Erodent	angular alumina (Al_2O_3)
Erodent size range	350 to 425 μm
Average diameter of the erodent	380 μm

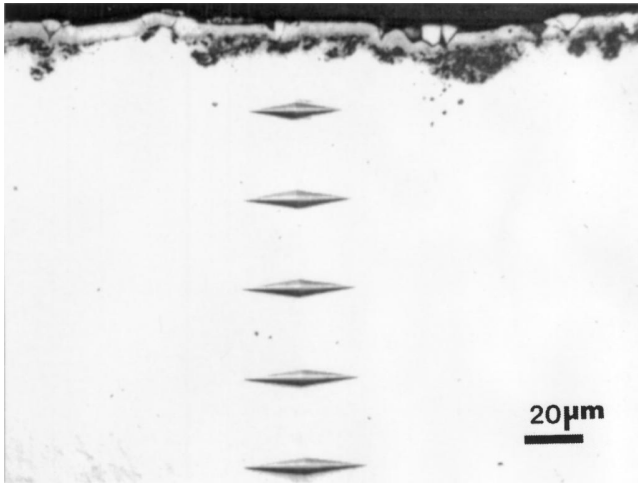


Fig. 2—Optical micrograph of a cross-sectional specimen used for microhardness measurements following erosion testing. Note the variation in hardness as the eroded surface is approached.

apparatus, with the specimen suspended within the furnace by a thermocouple wire wrapped around the sample. This thermocouple was also used to monitor the specimen temperature during heating. The incident and transmission bars are held outside the furnace during initial heating of the specimen and are mechanically slid into the furnace to lightly contact the specimen a few milliseconds before the incident-stress pulse impacts the sample. The initial specimen temperature was controlled to within ± 3 °C; however due to the adiabatic nature of the high-strain-rate experiments, a temperature rise occurred during deformation, which was detected in the output of the thermocouple. These deformation-induced temperature increases were determined to be relatively insignificant for the alloys and did not introduce any detectable thermal softening in the stress-strain response.

The microhardness measurements made on the eroded samples are quasi-static measurements of deformation that was introduced at high strain rates. In order to verify that these microhardness measurements could be correlated to the high-strain-rate constitutive behaviors measured from compression samples tested on the Hopkinson bars, an additional set of experiments was conducted. In these tests, compression specimens were first deformed on the Hopkinson bars at a high strain rate ($>2000/s$) to a true strain of approximately 0.2 and were then unloaded. These same samples were then remachined to right, regular cylinders and retested in compression under quasi-static conditions to determine the reload yield strength. If the reload yield strength measured under quasi-static conditions is similar to the flow-stress level at the end of the high-strain-rate compression test, then it could be assumed that the microhardness measurements taken from the eroded samples adequately reflect the flow-stress level introduced by the high-strain-rate deformation of the erosion process.

Finally, compression specimens of each material were deformed at several different combinations of strain rate and temperature, to various levels of strain, in order to produce a matrix of samples with a range of strengths. These samples were then sectioned, polished, and tested using the microhardness machine to develop a correlation between flow stress and hardness in the compression samples. This flow

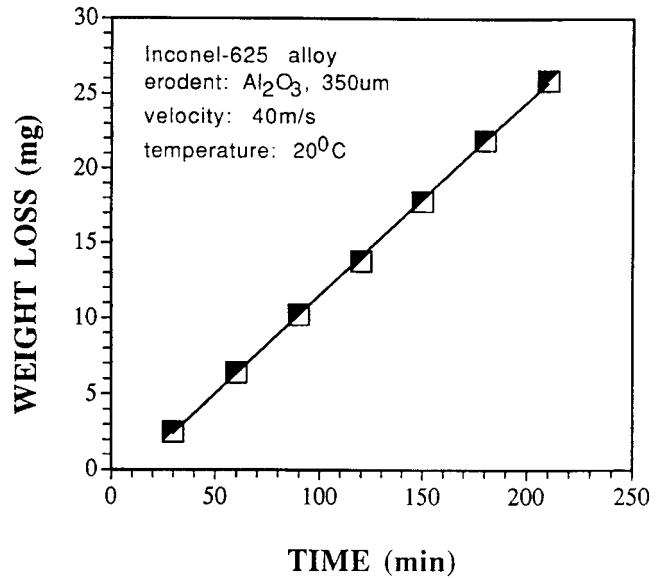


Fig. 3—Weight loss vs erosion time plot for the INCONEL-625 alloy. The slope of this represents the steady-state erosion rate.

stress/hardness correlation was then used to infer the strength of the materials below the eroded surfaces based on their microhardness readings.

III. RESULTS AND DISCUSSION

A. Erosion Tests and Plastic Deformation during Erosion

A typical weight loss vs time plot is presented in Figure 3 for solid-particle erosion of the INCONEL-625 alloy. The relative ranking of all the materials, based on their volumetric erosion rates, is listed in Table III. The INCONEL-625 alloy showed the lowest erosion rate of $0.0074 \text{ mm}^3/\text{min}$, while the Cu exhibited the highest erosion rate of $0.0104 \text{ mm}^3/\text{min}$. Results of the microhardness tests (Figure 4) showed that, for all the materials, the hardness significantly increased near the eroded surface. An increase in hardness indicates that the material beneath the eroded surface experienced plastic deformation, and, therefore, erosion resistance should be related to the ability of a material to *absorb* impact energy. The plastic-zone sizes for all alloys are listed in Table IV. It can be seen that copper has the largest plastic zone of $140 \mu\text{m}$, while the STELLITE-6 alloy has the smallest plastic zone of $20 \mu\text{m}$.

Table III. Volume Erosion Rates for Wrought Alloys at 90 Deg Particle Impact Angle

Alloy	Volume Erosion Rate (mm^3/min) $\times 10^3$
INCONEL-625	7.40 ± 0.07
Ultimet	7.54 ± 0.08
HASTELLOY-C22	7.80 ± 0.12
HAYNES-B3	7.80 ± 0.07
STELLITE-6	8.10 ± 0.05
316L SS	8.30 ± 0.05
Nickel	9.10 ± 0.15
Copper	10.4 ± 0.13

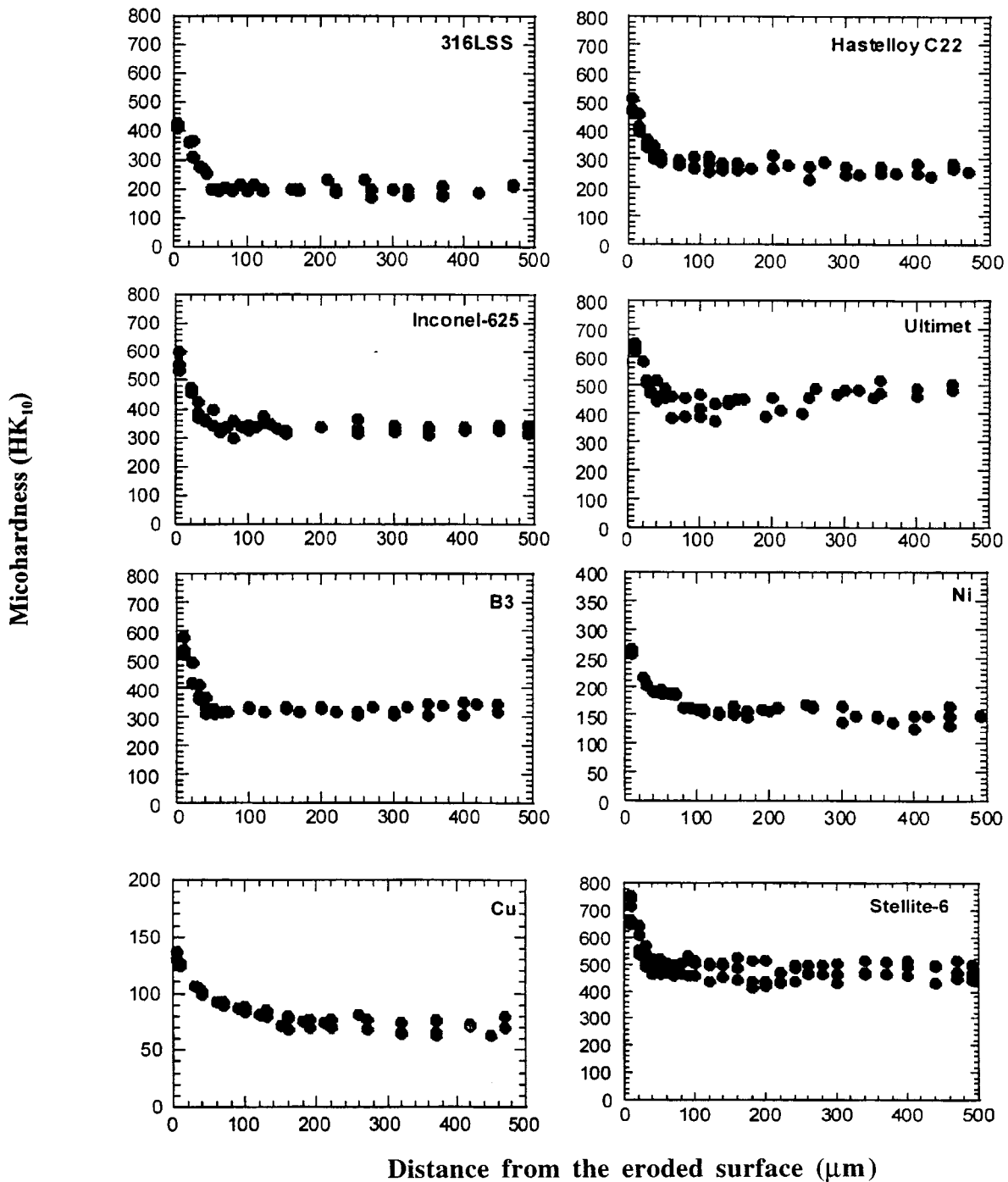


Fig. 4—Microhardness profiles obtained on the cross sections of the eroded samples after the longest exposure time (210 min).

B. Effect of Mechanical Properties on Energy Dissipation during Erosion

To consider the effect of the target material mechanical properties on erosion resistance, the following assumptions can be made to simplify the energy balance between an impacting particle and the target material: (1) the erodent particle is spherical and does not break upon impact, and (2) the temperature rise in the target during impact is not significant enough to cause change in its mechanical properties. The latter assumption appears to be reasonable for the erosion process, due to the small size of the impacting

particles and the comparatively large size of the target specimens. Therefore, the amount of energy converted to heat is insufficient to cause changes in the mechanical properties of the target material.

1. Plastic deformation energy

The kinetic energy of the particle before the impact is given by

$$KE = \frac{mV_i^2}{2} = KE_{pd} + KE_{ed} \quad [2]$$

where m is the mass of the particle, V_i is the initial velocity,

Table IV. Estimated Depth of Plastic Deformation Due to Erosion

Alloy	Plastic Zone Depth (μm)
Copper	140
Nickel	80
316L SS	60
INCONEL-625	50
HASTELLOY-C22	50
HAYNES-B3	40
Ultimet	40
STELLITE-6	20

and KE_{pd} and KE_{ed} are the plastic and elastic deformation energies, respectively. However, the portion of this energy transferred or delivered into the target material depends upon the mechanical properties of the target and erodent, such as the surface hardness, elastic modulus, etc. Upon impact, the kinetic energy of the particle transfers into (1) a rebound of the particle (KE_{ed}) and (2) plastic deformation of the target. The portion of the initial kinetic energy used for plastic deformation is equal to

$$KE_{pd} = \frac{mV_i^2}{2} - \frac{mV_r^2}{2} = \frac{mV_i^2}{2} \cdot \left[1 - \left(\frac{V_r}{V_i} \right)^2 \right] \quad [3]$$

where V_r , is the rebound velocity of the particle. The term V_r/V_i , referred to as the coefficient of restitution (e), represents the stored elastic energy in the particle and the target material after the impact. For example, if the coefficient of restitution is high (i.e., the rebound velocity is close to the incident velocity), the energy transferred to elastic deformation of the target would also be high, and, therefore, the target material would not experience significant plastic deformation. The coefficient of restitution depends on the mechanical properties of the particle and target materials (i.e., hardness and elastic modulus).

According to Lankov^[8] and Johnson,^[19] for spherical particles, the coefficient of restitution can be expressed as a function of the hardness and elastic modulus:

$$e = \left(\frac{V_r}{V_i} \right) = \frac{1.75 \cdot H^{5/8} \cdot J^{1/2}}{\rho_p^{1/8} \cdot V_i^{1/4}} \quad [4]$$

or

$$e^2 = \left(\frac{V_r}{V_i} \right)^2 = \frac{3.06 \cdot H^{5/4} \cdot J}{\rho_p^{1/4} \cdot V_i^{1/2}} \quad [5]$$

where ρ_p is the density of the impacting spherical particle in kg/m^3 , H is the target material hardness in N/m^2 , V_i is the initial particle velocity in m/s , and J is a parameter related to the elastic modulus and Poisson coefficients of the target and particle materials. The value of J is given by

$$J = \frac{(1 - \mu_t^2)}{E_t} + \frac{(1 - \mu_p^2)}{E_p} \quad [6]$$

where μ_t and μ_p are the Poisson coefficients of the target and particle materials, respectively, and E_t and E_p are the elastic modulus of the target and particle materials, respectively, in N/m^2 . Substitution of Eq. [6] into Eq. [5] gives

$$e^2 = \frac{(3.06 \cdot H^{5/4})}{(\rho_p^{1/4} \cdot V_i^{1/2})} \cdot \left[\frac{(1 - \mu_t^2)}{E_t} + \frac{(1 - \mu_p^2)}{E_p} \right] \quad [7]$$

Therefore, Eq. [3] can be rewritten as

$$KE_{pd} = \frac{mV^2}{2} \cdot \left[1 - \left(\frac{3.06 \cdot H^{5/4}}{\rho_p^{1/4} \cdot V_i^{1/2}} \right) \cdot \left(\frac{(1 - \mu_t^2)}{E_t} + \frac{(1 - \mu_p^2)}{E_p} \right) \right] \quad [8]$$

Equation 8 shows that, for a target material with a high hardness-to-modulus ratio, a larger portion of the incident particle's kinetic energy transforms into rebound kinetic energy when compared to materials with a low hardness. Therefore, the energy used for plastic deformation during erosion is lower for hard materials than for soft materials.

2. Erosion parameter

Bitter^[1] suggested that the erosion rate is proportional to the ratio of the input kinetic energy to the energy needed to remove a unit volume of the material. Based on this concept, the erosion rate of the material is proportional to the ratio of the energy used for plastic deformation and to the energy required to cause fracture (or, the fracture energy). A mechanical property that can represent the fracture energy per unit volume is the tensile toughness, or area under the true stress–true strain curve. The volume within which plastic deformation is absorbed during erosion is defined by the plastic-zone size. Now, the expression for the erosion parameter can be written as follows:

$$\text{Erosion rate} \propto E_{\text{parameter}} = \frac{mV^2}{2}$$

$$\left[\frac{1 - \left(\frac{3.06 \cdot H^{5/4}}{\rho_p \cdot V_i^{1/2}} \right) \cdot \left(\frac{(1 - \mu_t^2)}{E_t} + \frac{(1 - \mu_p^2)}{E_p} \right)}{T \cdot L} \right] \quad [9]$$

where $E_{\text{parameter}}$ is an erosion parameter, T is the tensile toughness of a material in J/m^3 , and L is the plastic-zone volume. A summary of all the terms in Eq. [9] is presented in Table V.

Equation [9] shows that, for the same erosion conditions (i.e., erodent velocity and density are constant), the $E_{\text{parameter}}$ is low for materials that combine a high hardness-to-modulus

Table V. Summary of the Terms Included in the Erosion Model (Equation [9])

Term	Definition	Units
$E_{\text{parameter}}$	erosion parameter	—
m	mass of the impacting particles	kg
V_i	initial particle velocity	m/s
H	target material hardness	N/m^2
ρ	density of the impacting spherical particle	kg/m^3
μ_p	Poisson coefficients of the particle material	—
μ_t	Poisson coefficients of the target material	—
E_p	elastic modulus of the particle material	N/m^2
E_t	elastic modulus of the target material	N/m^2
T	toughness	J/m^3
L	plastic zone volume	m^3

ratio and high tensile toughness. In addition, the proposed erosion parameter includes not only properties of the target material, but also properties of the erodent that contribute to the elastic and plastic deformation of the target. To evaluate the validity of Eq. [9], the tensile toughness of materials during erosion was estimated from the high-strain-rate compression tests. In addition, the maximum hardness measured beneath the eroded surface was substituted for H in Eq. 9. The plastic-zone volume was estimated from the surface area of the eroded samples (constant for all materials) and

the depth of the plastic deformation beneath the eroded surface, as determined by microhardness measurements. The procedure for estimating the mechanical properties during erosion is presented subsequently. It is worth noting here that, if it were possible to directly measure the coefficient of restitution of the impacting particles, it would then be possible to use Eq. [9] directly for determining the erosion parameter. However, direct measurement of the coefficient of restitution for very small particles presents a considerable experimental challenge.

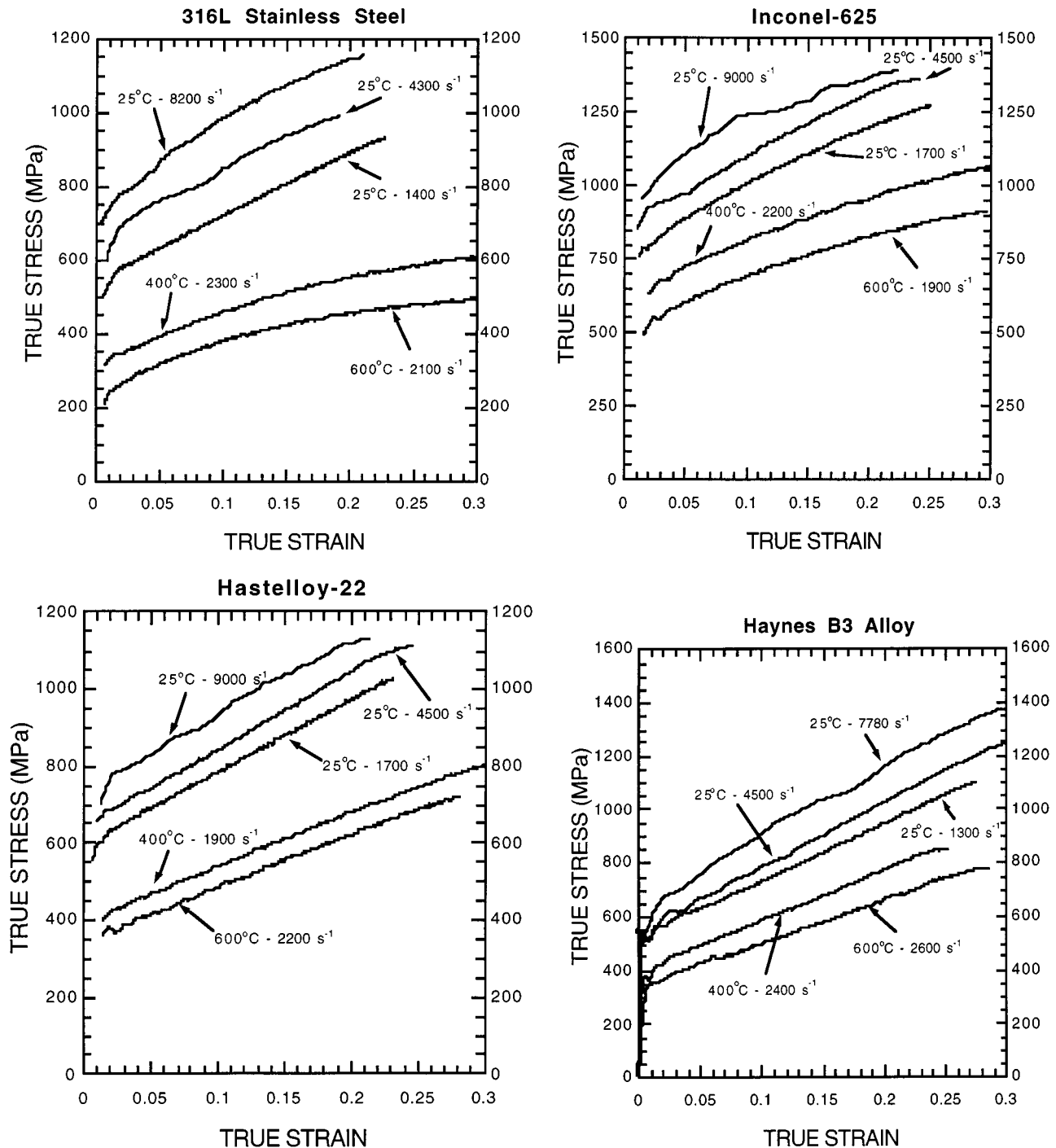


Fig. 5—Stress-strain curves generated for each material over a range of strain rates and test temperature. For each material, strain rate and test temperature have a pronounced influence on the yield and flow stress of the material.

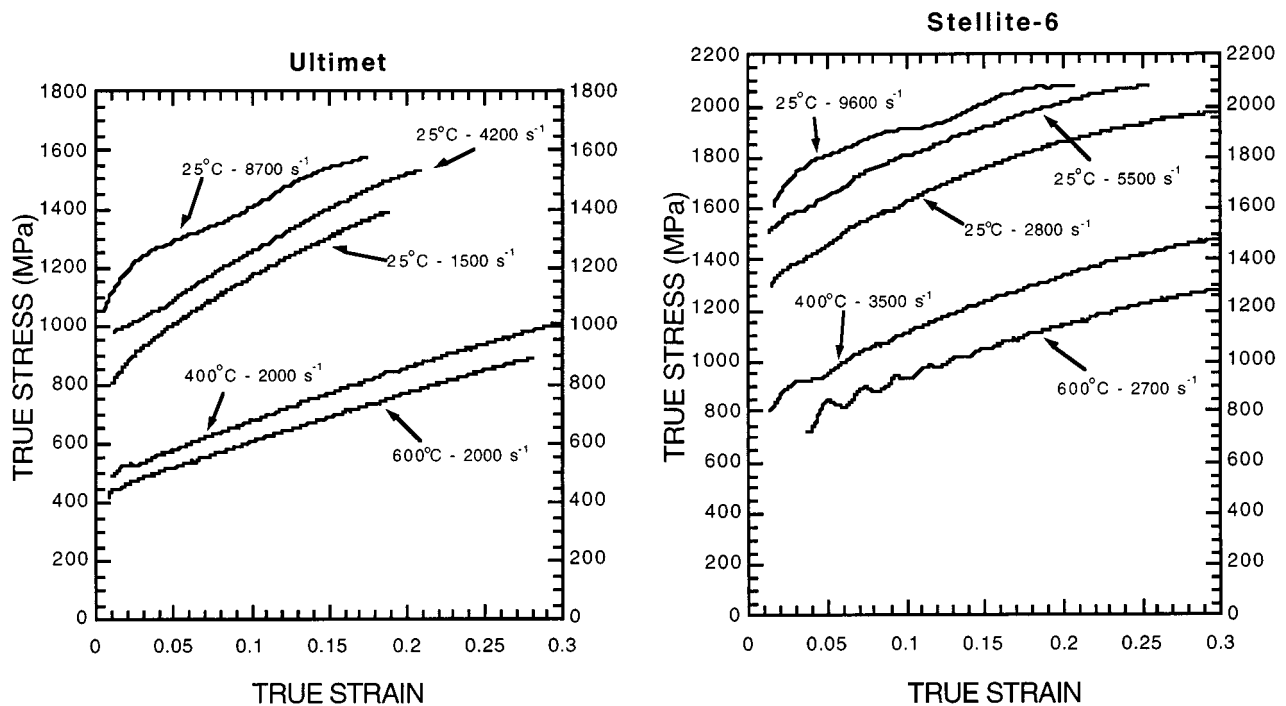


Fig. 5—(Continued) Stress-strain curves generated for each material over a range of strain rates and test temperature. For each material, strain rate and test temperature have a pronounced influence on the yield and flow stress of the material.

3. Mechanical properties during erosion

Knowing the tensile toughness of the material under the high-strain-rate and elevated-temperature deformation conditions associated with the erosion process is necessary in order to determine the erosion parameter calculated from Eq.[9]. High-strain-rate *tensile* tests require very specialized facilities, and no such tests have yet to be performed at elevated temperatures due to experimental difficulties. As such, a method was developed to make use of high-strain-rate compression tests, which are considerably easier to perform and can be done at elevated temperatures, to determine the tensile toughness of each material. To estimate the tensile toughness (T) associated with the erosion process, the following procedure was utilized: (1) compression stress-strain curves at strain rates comparable to those during erosion were generated using the compression Hopkinson bar; (2) the failure stress at the eroded surface was estimated from microhardness measurements of the eroded samples; (3) the failure strain was inferred from the failure stress and compressive stress-strain curves; and (4) the tensile toughness was determined by integration of the compression stress-strain curves over the strain range from zero to the failure strain.

4. High-strain-rate compression tests

Strain rates during solid-particle erosion are different from those during quasi-static mechanical tests. Depending on erosion conditions (*i.e.*, particle velocity, target temperature, and erodent size), strain rates in target materials may range between 10^3 and 10^7 s^{-1} . In contrast, quasi-static tests provide strain rates between 10^{-4} and 10^{-1} s^{-1} . Clearly, for rate-sensitive materials, *high-strain-rate* mechanical tests are necessary to develop accurate correlations between mechanical properties and erosion resistance. In this study, high-strain-rate compression tests were conducted at strain

rates of $\sim 10^3$ to 10^4 s^{-1} . These strain rates are similar to those calculated by Hutchings^[15] for particle impacts at 40 m/s. Therefore, mechanical properties measured from the high-strain-rate tests could be used as an estimate of the mechanical properties during erosion. Figure 5 shows stress-strain curves generated for each material over a range of strain rates and test temperatures. For each material, strain rate and test temperature have a pronounced influence on the yield and flow stress of the materials. In some of the materials, the flow-stress level at high strain rates may be twice that associated with quasi-static conditions. The difference in tensile toughness for each material is, therefore, very dependent on both the target temperature and strain rate associated with the erosion process.

Figure 6 shows the stress-strain curves for materials which had been first tested at a high strain rate at room temperature then reloaded at a low strain rate, to determine if a quasi-static test (such as the hardness tests) conducted following a high-strain-rate experiment accurately predicts the flow-stress level achieved during the previous high-strain-rate tests. Since the quasi-static reload yield point is close to the flow stress at the end of the high-strain-rate test, it is reasonable to assume that the hardness measurements of the erosion samples reasonably reflect the flow-stress levels achieved during erosion. The slightly lower quasi-static reload-stress level arises due to recovery following the high-strain-rate test, as a result of adiabatic heating associated with the dynamic deformation. The lower reload stress is present even if the sample was reloaded dynamically at the same high strain rate, verifying the recovery effect.

5. Estimation of tensile toughness during erosion

For eroded materials, the failure strength can be estimated from the microhardness profiles beneath the eroded surface.

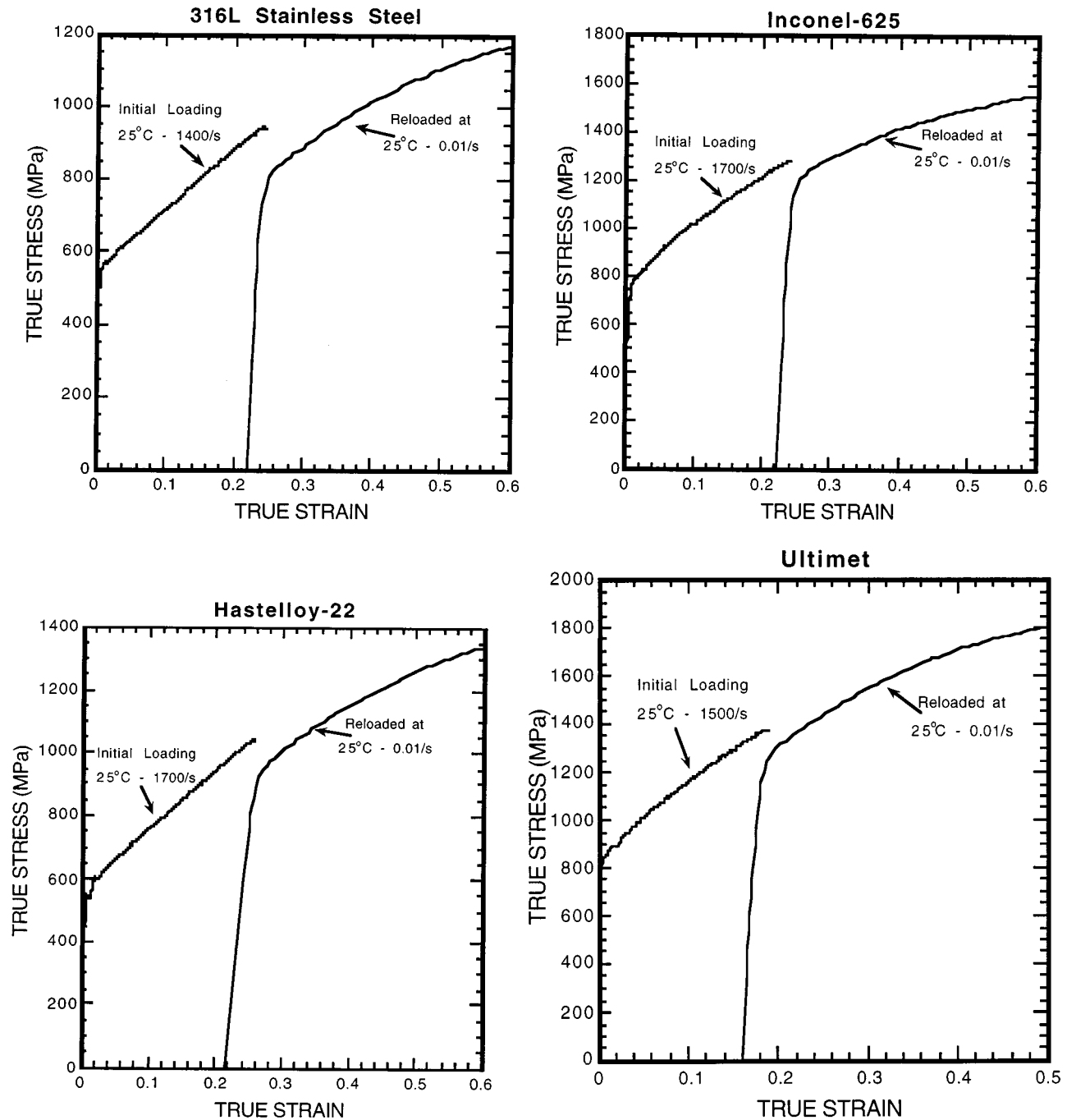


Fig. 6—Stress-strain curves of several of the materials, which were first tested at high strain rate at room temperature and then reloaded at low strain rate.

During particle impact, when the yield strength of the material is locally exceeded, plastic deformation takes place in the vicinity of the impact. After multiple impacts, a plastically deformed surface layer may form near the eroded surface, and, therefore, the yield strength of the material increases due to strain hardening. Upon further deformation, the yield strength at the surface will eventually become equal to its fracture strength, and no further plastic deformation will occur. At this point, the surface becomes brittle and its fragments may be removed by the subsequent impacts. The hardness of the material at the eroded surface may be used as an estimate of its fracture strength, written as

$$H = A\sigma_f^{[20]} \quad [10]$$

where H is the hardness, σ_f is the fracture strength, and A is a constant which can be experimentally determined from microhardness measurements conducted on compression samples. To estimate failure strength during erosion, 10 g Knoop microhardness tests were conducted on both high-strain-rate compression samples and cross sections of the eroded alloys. Using known stress values from the high-strain-rate compression curves (Figure 5) and corresponding hardness values, the constant A was determined using Eq. [10]. Subsequently, the constant A was used to calculate the failure strength from the microhardness measurements near the eroded surface ($5 \mu\text{m}$ from the surface). Results of the hardness-stress conversion are shown in Table VI. Once the

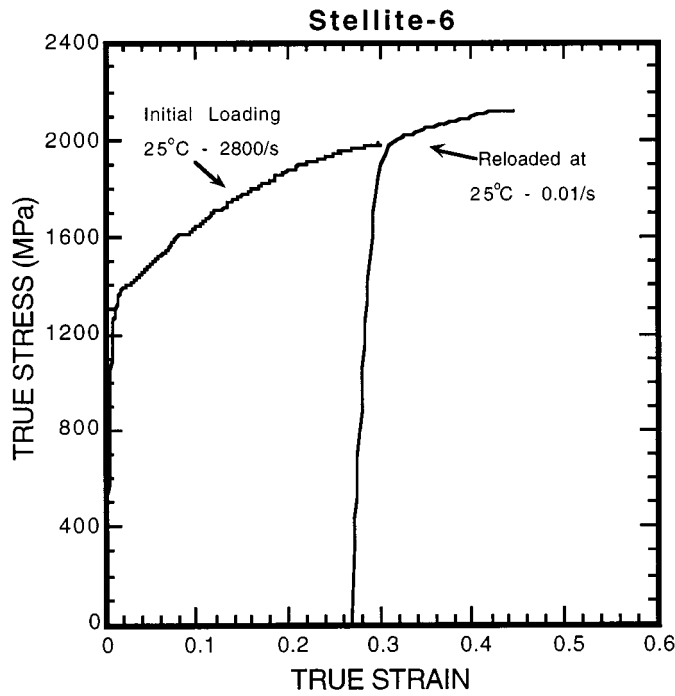


Fig. 6—(Continued) Stress-strain curves of several of the materials, which were first tested at high strain rate at room temperature and then reloaded at low strain rate.

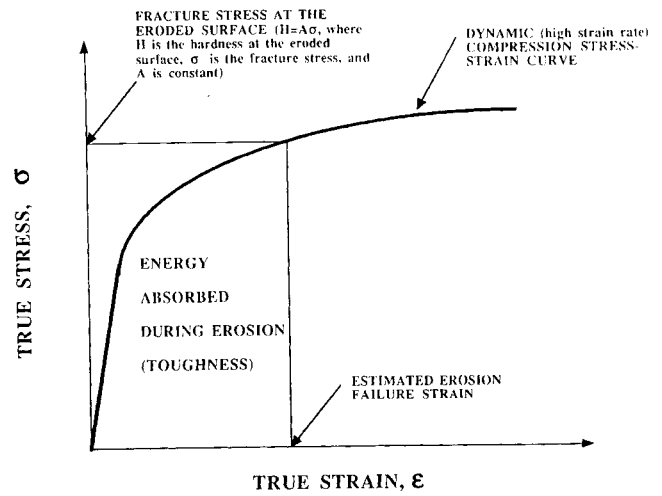


Fig. 7—Schematic diagram showing the procedure that was used to estimate tensile toughness during erosion using high-strain-rate compression and microhardness tests.

fracture strength was determined, the fracture strain and toughness were found from the high-strain-rate compression stress-strain curves. Toughness was determined by integrating the stress-strain relationship between a 0.02 strain (yielding) and the failure strain. A schematic illustration of this procedure is shown in Figure 7. Estimated failure

Table VI. Hardness-Strength Conversion ($H = A \cdot \sigma_f$)^[20]

Alloy	Strain Rate (s ⁻¹)	Stress (MPa)	Hardness, <i>H</i> (10 g Knoop) (MPa) ^a	Constant, <i>A</i> = <i>H</i> / σ (Average Value)	Hardness at the Eroded Surface (10 g, Knoop) (MPa)	Failure Strength at the Eroded Surface (MPa)
Ultimet	1500	1350	5030 ± 360	3.7	6330 ± 200	1710 ± 60
	4200	1500	5500 ± 430	3.7 (3.7)		
	8700	1600	6000 ± 360	3.7		
INCONEL-625	1700	1250	4410 ± 530	3.5	5660 ± 280	1664 ± 82
	4500	1350	4580 ± 220	3.4 (3.4)		
	9000	1400	4740 ± 260	3.4		
HASTELLOY-C22	1700	1050	3840 ± 230	3.7	4860 ± 230	1314 ± 62
	4500	1100	4465 ± 280	4.0 (3.7)		
	9000	1160	4150 ± 240	3.6		
316L SS	1400	900	3410 ± 260	3.8	4270 ± 100	1186 ± 31
	4300	1000	3750 ± 290	3.8 (3.6)		
	8200	1150	3820 ± 260	3.3		
HAYNES-B3	1300	1095	4290 ± 280	3.6	5560 ± 330	1463 ± 87
	4500	1248	4600 ± 270	3.7 (3.8)		
	7800	1392	4930 ± 320	3.9		
STELLITE-6	2800	1950	6640 ± 510	3.4	7200 ± 500	1945 ± 135
	5500	2050	7610 ± 470	3.7 (3.7)		
	9600	2050	7880 ± 770	3.8		
Copper	2500	345	1250 ± 60	3.7 (3.7)	1250 ± 50	338 ± 14
	4500	350	1310 ± 110	3.6		
Nickel ^b	—	—	—	3.5	2560 ± 150	731 ± 43

^aHardness numbers and standard deviations were calculated from at least ten indentations.

^bSince in this study no high-strain-rate tests were performed for nickel, the value for constant *A* was approximated as 3.5, and failure strain and toughness were estimated from the high-strain-rate stress-strain curves found in the literature (P.S. Follansbee *et al.*: *Acta Metall. Mater.*, 1990, vol. 38 (7), pp. 1241-54).

Table VII. Estimated Failure Strength, Failure Strain, and Tensile Toughness Values during Erosion

Alloy	Strain Rate (s ⁻¹)	Stress-Strain Relationship* $\sigma = \sigma_0 + K\epsilon^n$	Failure Strength, σ_f (MPa)	Failure Strain, ϵ_f	Toughness M J/m ³
Ultimet	8700	$804 + 1926\epsilon^{0.55}$	1710 ± 60	0.25 ± 0.02	355 ± 43
IN-625	9000	$830 + 1600\epsilon^{0.6}$	1664 ± 82	0.31 ± 0.05	416 ± 84
C22	9000	$613 + 1200\epsilon^{0.54}$	1314 ± 43	0.35 ± 0.05	370 ± 65
316L SS	8200	$684 + 1208\epsilon^{0.59}$	1186 ± 31	0.22 ± 0.02	220 ± 22
HAYNES-B3	7800	$508 + 1940\epsilon^{0.68}$	1463 ± 87	0.35 ± 0.05	375 ± 70
STELLITE-6	9600	$1500 + 1800\epsilon^{0.57}$	1945 ± 135	0.091 ± 0.045	167 ± 89
Copper	4500	$20 + 693\epsilon^{0.6}$	338 ± 14	0.27 ± 0.02	57 ± 5
Nickel**	4000	$50 + 1298\epsilon^{0.5}$	731 ± 43	0.32 ± 0.04	158 ± 30

* σ_0 is the yield strength and K is the strength coefficient.

**The stress-strain relationship was obtained from P.S. Follansbee *et al.*: *Acta Metall. Mater.*, 1990, vol. 38 (7), pp. 1241-54.

strength, failure strain, and tensile toughness values during erosion are listed in Table VII.

6. Effect Of Mechanical Properties On Erosion Resistance

In this study, the erosion test conditions were kept the same for all the materials ($V_i = 40$ m/s, $E_p = 400 \times 10^9$ N/m², $\mu_p = 0.21$, $\mu_t = 0.35$, and $\rho_p = 4000$ kg/m³). All the tested materials have similar modulus values ($E_t = 210 \times 10^9$ N/m²), with the exception of copper ($E_t = 130 \times 10^9$ N/m²). Thus, tensile toughness, maximum hardness near the eroded surface, and plastic-zone volume values can be used to examine the validity of Eq.[9] for the erosion parameter and to determine the combined effects of hardness and toughness on erosion resistance. The calculated erosion parameter from Eq. [9] is plotted against the experimentally determined volumetric erosion rates in Figure 8. It can be seen that a decrease in values of the erosion parameter leads to a

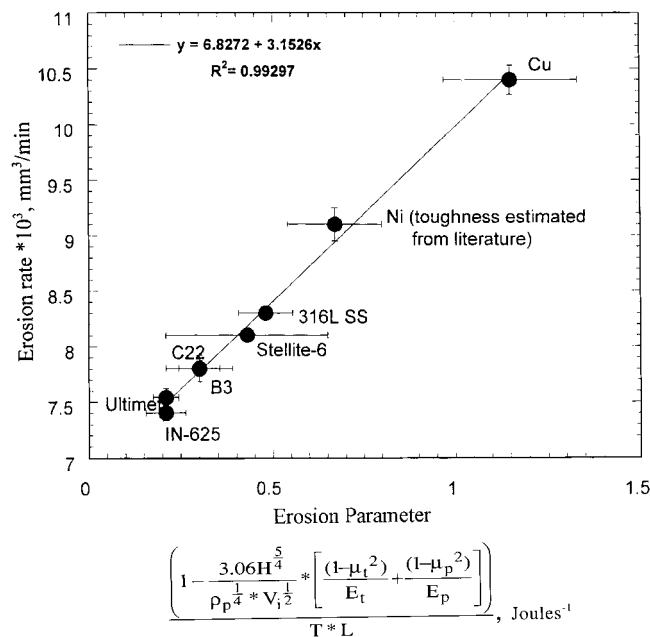


Fig. 8—The erosion parameter (excluding the initial kinetic energy term) calculated from Eq. [9] is plotted against the experimentally determined volumetric erosion rate. Good correlation is observed for the range of materials studied here.

decrease in erosion rates. This plot shows that materials combining high hardness and high toughness at high strain rates have low values of $E_{parameter}$ and, therefore, may offer good erosion resistance. Hardness is necessary to reduce the energy transferred from the incident particle into the material, and toughness is indicative of the ability of the material to absorb this energy without fracture. However, high hardness may reduce the ability of the material to deform plastically and, therefore, its toughness may decrease. The optimum combination of these properties provides the best erosion resistance. The large scatter in the calculated erosion parameter for the STELLITE-6 alloy is associated with the error in microhardness measurements. This alloy contains a large volume fraction of carbides within a ductile matrix, which affects microhardness measurements in the matrix and causes significant scatter in the data.

If a ductile material is not strain-rate sensitive, its quasi-static mechanical properties can be correlated to erosion resistance. However, for the most ductile materials, their mechanical properties at high strain rates are different from their quasi-static properties. Since solid-particle erosion involves high-strain-rate deformation of the target material, caution must be taken when a relationship between quasi-static mechanical properties and erosion resistance is drawn. Unfortunately, the exact strain rates during erosion are difficult to estimate because of the gradual change in mechanical properties with distance from the eroded surface. However, as was shown here, compression tests at high strain rates can provide a reasonable estimate of the mechanical properties during erosion and can be used to predict the erosion behavior of materials.

IV. CONCLUSIONS

The deformation behavior and erosion resistance of ductile Ni-, Co-, and Fe-based alloys were analyzed. High-strain-rate mechanical tests, along with microhardness tests, were used to estimate the mechanical properties of these materials during erosion. Based on the results of this study, the following can be concluded.

1. An erosion parameter was developed based on considerations of energy loss during erosion that showed good correlation to experimentally measured erosion rates.
2. Materials combining high hardness and tensile toughness

at high strain rates showed good erosion resistance. Hardness is necessary to reduce energy transferred from the particle into the material, and toughness is indicative of the ability of the material to absorb this energy without fracture.

3. A procedure for the estimation of the mechanical properties of the material during erosion, using high-strain-rate compression tests and microhardness measurements, was developed. High-strain-rate compression tests can also be conducted at elevated temperatures to more accurately estimate mechanical properties of materials under the specific conditions associated with solid-particle erosion.

ACKNOWLEDGMENTS

The authors acknowledge the financial support of Ohio Edison Co., Pennsylvania Power & Light Co., Centerior Energy Co., Public Service Electric & Gas Co., Virginia Power Co., Allegheny Power Co., Delmarva Power Co., and United States Department of Energy under Grant No. DE-FG22-95PC95211. The authors also thank A.O. Bencotter and B. Lindsley for their help in the sample preparation and erosion tests. KSV acknowledges the financial support of Haynes International (Kokomo, IN) for this work. The authors extend special thanks to Aashish Rohatgi and Jon Isaacs for their assistance in the high-strain-rate testing.

REFERENCES

1. J.G.A. Bitter: *Wear*, 1963, vol. 6, pp. 5-21.
2. G. Sundararajan and P.G. Shewmon: *Wear*, 1983, vol. 84, pp. 237-58.
3. A. Ball: *Wear*, 1983, vol. 91, pp. 201-07.
4. I. Finnie, J. Wolak, and Y. Kabil: *J. Mater.*, 1967, vol. 2, p. 682.
5. A. Levy and Jahanmir: *Corrosion-Erosion Behavior of Materials*, K. Natesan, ed., TMS-AIME, New York, NY, 1980, p. 177.
6. B.F. Levin, J.N. DuPont, and A.R. Marder: *Wear*, 1995, vols. 181-183, pp. 810-20.
7. I.M. Hutchings: *J. Appl. Phys.*, 1986, vol. 25, pp. A212-A221.
8. A.A. Lankov: *Trenie Iznos (Russian)*, 1992, vol. 25, pp. 206-21.
9. I.M. Hutchings: *Wear*, 1981, vol. 13 (1), pp. 269-81.
10. I. Finnie: *Wear*, 1960, vol. 3, pp. 87-103.
11. W.J. Head and M.E. Harr: *Wear*, 1970, vol. 15, pp. 1-46.
12. S. Soderberg, S. Hogmark, and H. Swahn: *ASLE Trans.*, 1982, vol. 26 (2), pp. 161-72.
13. A.V. Reddy, G. Sundararajan, R. Sivakumar, and P. Rama Rao: *Acta Metall.*, 1984, vol. 32, pp. 1305-16.
14. A.V. Reddy and G. Sandararajan: *Wear*, 1986, vol. 111, pp. 313-23.
15. I.M. Hutchings: *J. Phys. D: Appl. Phys.*, 1977, vol. 10, p. L179.
16. B. Lindsley, K. Stein, and A.R. Marder: *Measurement Sci. Technol.*, 1995, vol. 6, p. 1169.
17. P.S. Follansbee: in *Metals Handbook*, 9th ed., ASM, Metals Park, OH, 1985, vol. 8, pp. 198-203.
18. S. Nemat-Nasser, J.B. Isaacs, and J.E. Starrett: *Proc. R. Soc. London*, 1991, vol. A435, pp. 371-99.
19. K.L. Johnson: *Contact Mechanics*, Cambridge University Press, Cambridge, United Kingdom, 1985, p. 363.
20. D. Tabor: *The Hardness of Metals*, Clarendon Press, Oxford, United Kingdom, 1951.